Acta Pharmaceutica Sinica B 2024;14(9):4073–4086

Chinese Pharmaceutical Association
Institute of Materia Medica, Chinese Academy of Medical Sciences

Acta Pharmaceutica Sinica B

www.elsevier.com/locate/apsb
www.sciencedirect.com

ORIGINAL ARTICLE

An iron-based metal-organic framework nanoplatform for enhanced ferroptosis and oridonin delivery as a comprehensive antitumor strategy

Mengru Cai, Tingting Fu, Rongyue Zhu, Panxiang Hu, Jiahui Kong, Shilang Liao, Yuji Du, Yongqiang Zhang, Changhai Qu, Xiaoxv Dong, Xingbin Yin*, Jian Ni*

School of Chinese Materia Medica, Beijing University of Chinese Medicine, Beijing 102488, China

Received 7 February 2024; received in revised form 30 April 2024; accepted 7 May 2024

KEY WORDS

Metal-organic frameworks;
Immunotherapy;
Self-amplifying ferroptosis;
Photodynamic therapy;
Chemodynamic therapy;
Oridonin;
Fused cell membrane coating;
Metabolization

Abstract Ferroptosis is a recently discovered pathway for regulated cell death pathway. However, its efficacy is affected by limited iron content and intracellular ion homeostasis. Here, we designed a metal-organic framework (MOF)-based nanoplatform that incorporates calcium peroxide (CaO_2) and oridonin (ORI). This platform can improve the tumor microenvironment and disrupt intracellular iron homeostasis, thereby enhancing ferroptosis therapy. Fused cell membranes (FM) were used to modify nanoparticles (ORI@CaO_2@Fe-TCPP, NPs) to produce FM@ORI@CaO_2@Fe-TCPP (FM@NPs). The encapsulated ORI inhibited the HSPB1/PCBP1/IREB2 and FSP1/COQ10 pathways simultaneously, working in tandem with Fe^{3+} to induce ferroptosis. Photodynamic therapy (PDT) guided by porphyrin (TCPP) significantly enhanced ferroptosis through excessive accumulation of reactive oxygen species (ROS). This self-amplifying strategy promoted robust ferroptosis, which could work synergistically with FM-mediated immunotherapy. *In vivo* experiments showed that FM@NPs inhibited 91.57% of melanoma cells within six days, a rate 5.6 times higher than chemotherapy alone. FM@NPs were biodegraded and directly eliminated in the urine or faeces without substantial toxicity. Thus, this study demonstrated that combining immunotherapy with efficient ferroptosis induction through nanotechnology is a feasible and promising strategy for melanoma treatment.

*Corresponding authors.
E-mail addresses: yxbtcm@bucm.edu.cn (Xingbin Yin), 602054@bucm.edu.cn (Jian Ni).

Peer review under the responsibility of Chinese Pharmaceutical Association and Institute of Materia Medica, Chinese Academy of Medical Sciences.

https://doi.org/10.1016/j.apsb.2024.05.015

1. Introduction

The global incidence of melanoma, one of the most malignant tumors, is on the rise[1,2]. Currently, the treatment modalities for melanoma encompass surgical resection, radiotherapy, and chemotherapy[3–5]. However, these treatments are associated with significant drawbacks, such as significant side effects, development of drug resistance, and high treatment costs[6]. Therefore, the treatment of melanoma remains a formidable challenge, and the use of multifunctional targeting agents could potentially enhance therapeutic outcomes. Ferroptosis is an iron-dependent form of cell death characterized by the accumulation of reactive oxygen species (ROS) and lipid peroxides (LPO)[7]. Key mechanisms in ferroptosis include glutathione (GSH) depletion, glutathione peroxidase 4 (GPX4) inactivation, and Fe^{2+} accumulation[8–9]. However, insufficient intracellular iron content and homeostasis limit the clinical application of ferroptosis.

Oridonin (ORI), a naturally occurring terpenoid compound, has been extensively researched as a novel anti-tumor drug[10]. Although ORI has not yet been approved for clinical anti-tumor therapy, numerous studies have explored its anti-tumor application. ORI has demonstrated improved anti-tumor efficacy and chemotherapy resistance in combination with paclitaxel, doxorubicin, and 5-fluorouracil while exhibiting low toxicity[11–16]. Several reliable mechanisms have been proposed to explain the anticancer effects of ORI[17]. One of the most widely accepted mechanisms is that ORI induces ferroptosis in tumor cells by reducing the activity of GPX4 and consuming intracellular GSH[18–20]. Nevertheless, it is usually difficult to obtain satisfactory therapeutic effects with monotherapy owing to the heterogeneity and complexity of tumors[21]. Monotherapy is usually associated with poor prognosis of tumors, with metastasis and recurrence being common. Moreover, non-specific tissue distribution of drugs often leads to low drug concentrations at tumor sites and significant toxicity in normal tissues[22]. One effective approach is to integrate multiple treatment methods into a single platform[23].

Nanomedicines are attractive paradigms for drug delivery that can efficiently overcome various biological barriers and substantially improve drug delivery efficiency, tumor-targeting ability, and imaging sensitivity[24]. Metal-organic frameworks (MOFs) are self-assembled inorganic-organic hybrid materials composed of metal link centres and polydentate bridging ligands. These frameworks are attractive multimodal therapeutic platforms. In particular, Fe-porphyrin MOF, which are inorganic-organic hybrid nanoparticles formed by the self-assembly of Fe-ions and the photosensitizer porphyrin, have been widely studied owing to their therapeutic effect[25–27]. Among them, Fe-TCPP (FT), a typical MOF, contains tetrakis (4-carboxyphenyl) porphyrin (TCPP), a photosensitizer that induces photodynamic therapy (PDT), and Fe^{3+}, which initiates chemodynamic therapy (CDT) and is non-toxic. The delivery of ORI *via* FT for anti-tumor therapy can further aggravate intracellular iron overload and reduce GSH content, presenting an attractive treatment strategy for ferroptosis. More importantly, PDT may act synergistically with CDT to boost treatment efficacy and prevent multidrug resistance[28].

To date, key strategies for augmenting PDT and CDT have involved increasing intracellular O_2 content and H_2O_2 levels while depleting GSH. These steps overcome the limitations of endogenous H_2O_2 deficiency and low O_2 content in tumor cells. In this study, a biocompatible nanoparticle calcium peroxide (CaO_2) has been proposed for hybrid growth with an iron porphyrin MOF. CaO_2 is considered to have high biological safety because of its ability to continuously release O_2 and H_2O_2[29]. Given that CaO_2 simultaneously produces both O_2 and H_2O_2, it has obvious efficacy as an enhancer of PDT and CDT during the treatment of hypoxic solid tumors. Simultaneously, CaO_2 causes calcium overload by releasing Ca^{2+} into cells[30]. Calcium overload has been linked to tumor death, and cancer cells exhibit greater sensitivity to increased Ca^{2+} concentration compared to normal cells[31]. Hence, CaO_2 provides Ca^{2+} in an ion-interference therapeutic strategy while improving the tumor microenvironment by boosting the levels of O_2 and H_2O_2. This represents an excellent integration of PDT, CDT, and ion interference therapy.

More importantly, the prognosis of conventional tumor treatments is poor due to metastasis and recurrence[32]. Immunotherapy has shown unique advantages in persistently suppressing tumors, and its combination with other treatment modalities may expand the efficacy of tumor treatment[33]. The immunogenic cell death (ICD) of tumor cells induced by phototherapy and bioactive nanoparticles triggers a series of cellular responses by releasing tumor-associated antigens and damage-associated molecular patterns, which ultimately activate innate and adaptive immune responses[34]. However, the identified tumor antigens are insufficient to support optimal immunotherapy. The fusion of tumor cells with dendritic cells (DCs) enables the expression of intact tumor antigens on hybrid cell membrane[35]. These hybrid cells also induce immune responses by expressing co-stimulatory molecules derived from DCs[36]. To date, various immunotherapeutic nano adjuvants have been developed using immune cells and their derived components as tumor-targeted delivery carriers[37–39]. Altogether, the construction of a multifunctional nano platform that can not only deliver a high dose of iron but also consume GSH to achieve efficient ferroptosis induction and deliver ORI *via* FT is warranted.

In this study, we designed a ferroptosis-inducing nano platform using iron-based MOF that combines iron supply and GSH consumption. CaO_2 was coated with a nanoscale MOF (Fe-TCPP, FT) layer using a seed growth strategy to prevent early leakage of CaO_2 into the blood circulation. In addition, inadequate iron supply inside solid tumors impedes the application of ORI as an anticancer drug. The current methods involve loading ORI onto Fe-containing nanocarriers for Fe-mediated cancer therapy. Thus, the core-shell CaO_2@FT was constructed as a carrier of ORI, and the hybrid cell membrane was modified on the surface to achieve targeted immunotherapy. When the FM@NPs reached the tumor site, the external FT layer dissolved in the weakly acidic microenvironment at the tumor site, where Fe^{3+} was further reduced to Fe^{2+} by the high concentration of GSH, resulting in the collapse of the frame structure. The breakdown of the FT led to the exposure of CaO_2, the

release of ORI, and the activation of the photosensitizer TCPP, which enabled synergistic Fe^{2+}-mediated chemokinetic therapy (CDT), ORI-mediated ferroptosis, Ca^{2+}-mediated oncosis therapy, and TCPP-mediated PDT (Scheme 1). The FM@NPs can cooperate with multiple therapeutic effects such as CDT, PDT, immunotherapy, and ferroptosis therapy and possess superior therapeutic efficiency *in vitro* and *in vivo*. Eventually, the FM@NPs would be excreted through the kidneys in the form of urine without causing actual toxicity.

2. Materials and methods

2.1. Materials

$FeCl_3 \cdot 6H_2O$, $CaCl_2$, oridonin, and TCPP were purchased from Shanghai Yuanye Bio-Technology Co., Ltd. (Shanghai, China). Gibco high-rich glucose 1640 was purchased from Thermo Fisher Scientific Co., Ltd. (Waltham, MA, USA). Fetal bovine serum (FBS) and a 1% penicillin-streptomycin mixture were acquired from Biodi Biotechnology Co., Ltd. (Beijing, China). Furthermore, 2′,7′-dichlorofluorescin diacetate (DCFH-DA), Annexin V-FITC/PI apoptosis assays kit, Calcien AM, and propidium iodide (PI) were purchased from Beyotime Institute of Biotechnology (Nanjing, China). Cell counting kit-8 (CCK-8) was obtained from Biorigin Inc. (Beijing, China). A reactive oxygen species assay kit was purchased from LABLEAD Inc. (Beijing, China).

2.2. Synthesis of ORI@CaO_2@FT (NPs)

The ORI@CaO_2@FT (NPs) were synthesized using a self-templating method. In this process, 3 mL of the TCPP ethanol solution (1 mg/mL), 6 mL of the ORI ethanol solution (15 mg/mL), and 6 mL of the CaO_2 ethanol dispersion (3 mg/mL) were mixed and stirred vigorously for 5 min. Then, 3 mL of $FeCl_3 \cdot 6H_2O$ (5 mg/mL) ethanol solution was added. After stirring for 30 min at room temperature, the product was washed with ethanol and purified *via* centrifugation at 10,000 rpm for 5 min (Baiyang Medical Equipment Co., Ltd., Beijing, China). The resulting ORI@CaO_2@FT was redispersed in ethanol prior to use.

2.3. Preparation of FM@NPs

The NPs solution was ultrasonically mixed with the FM solution, and the mixture was centrifuged to obtain FM@NPs.

2.4. In vivo anticancer therapy

Animal experiments were conducted according to the guidelines approved by the Institutional Animal Care and Use Committee of the Beijing University of Chinese Medicine (BUCM-1-2021112001-0003). The B16-F10 tumor-bearing C57BL/6J mice were randomly divided into 17 groups, which were given different preparations, each at a dose of 15 mg/kg. Body weight and tumor size (tumor volume = $W^2 \times L/2$) were measured daily and recorded.

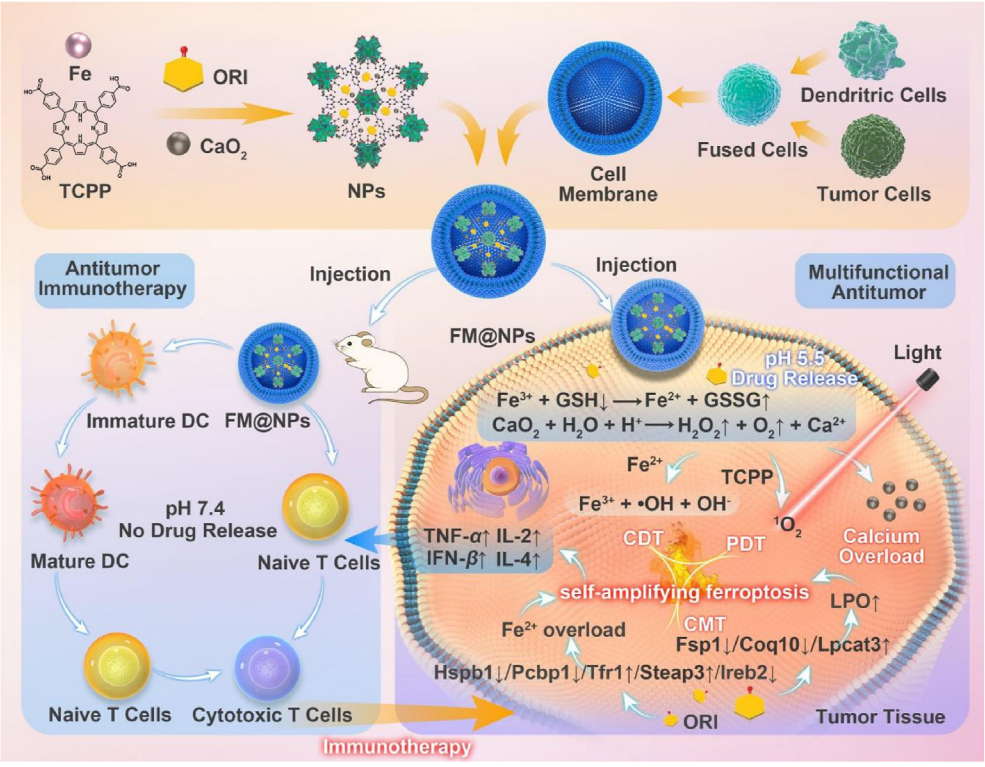

Scheme 1 Schematic illustration of an iron-based metal-organic framework nanoplatform for enhanced ferroptosis therapy as a comprehensive antitumor strategy.

More detailed experimental details are included in the Supporting Information.

3. Result and discussion

3.1. Synthesis and characterization of FM@ORI@CaO_2@Fe-TCPP (FM@NPs)

The fabrication of nanoscale FM@NPs is depicted in Scheme 1. First, the fused cell membrane (FM) was obtained as per previous reports[40]. To verify the successful fusion of the two cell lines, B16-F10 nuclei (B16-F10 is a cell line exhibiting a morphology of spindle-shaped and epithelial-like cells isolated from the skin tissue of a mouse with melanoma) were labelled with blue fluorescence Hoechst 33−342, while the cell membranes of DCs were stained with green fluorescence using 3,3'-octacosylate perchlorate (DIO). Confocal laser scanning microscopy (CLSM) revealed that the fused cells contained both blue nuclei and green membranes (Supporting Information Fig. S1), thereby confirming the successful fusion of DCs and B16-F10 cells. Next, a self-templating method was employed to synthesize ORI@CaO_2@Fe-TCPP (NPs)[41]. In this method, CaO_2 was incorporated into FT *via* nucleation to obtain CaO_2@FT. Tumor-targeting nanoscale FM@NPs were prepared by cloaking the NPs with FM under ultrasound in an ice bath[35]. B16-F10 cell-membrane-coated CM@NPs and DC-cell membrane-coated DM@NPs were prepared similarly. Different drug delivery systems (DDSs) were examined using scanning electron microscopy (SEM, Supporting Information Fig. S2) and transmission electron microscopy (TEM, Fig. 1A). As shown by TEM-EDS (Fig. 1B), the FM@NPs were well-dispersed core-shell nanospheres. After coating the cell membrane, the size of the FM@NPs was increased slightly (Fig. 1C), and the zeta potential changed from positive to negative (Fig. 1D). Changes in the size of the DDSs were examined in water and in a medium containing 10% serum, and it was discovered that the different DDSs had good stability for seven days (Supporting Information Fig. S3). This is useful for improving the safety of DDSs in the blood circulation. There were no significant differences in ultraviolet-visible spectroscopy (Fig. 1E) or fluorescence spectra (Fig. 1F) of the DDSs before and after cell membrane coating, indicating that the effect of the cell membrane coating on the NPs was negligible.

3.2. Cascade reactions investigation

As shown in Fig. 1G, the formation of hydroxyl radicals (·OH) was measured at a wavelength of 652 nm using the TMB method[42]. GSH induced the reduction of Fe^{3+} to Fe^{2+} in the subsequent Fenton-like reactions. However, the absorbance values of TMB were different. CaO_2@FT (CaO_2@FT) and the NPs showed the highest absorbance, followed by FM@NPs, whereas FT and ORI@FT (ORI@FT) showed the weakest absorbance. These results indicate that the presence of CaO_2 is beneficial for iron cycling and enhancement of the Fenton-like reaction. The efficiency of singlet oxygen generation by the different DDSs was evaluated using a DPBF probe (Fig. 1H). The results showed that different DDSs promoted the photodegradation of DPBF. In addition, the efficiency of the NPs in enhancing the generation of singlet oxygen ($^1O_2$) was slightly improved in the presence of CaO_2. The $^1O_2$ generation efficiencies of CaO_2@FT, NPs, DM@NPs, CM@NPs and FM@NPs were 53.19%, 54.55%, 57.28%, 49.10%, and 55.92%, respectively. These values were slightly higher than those for FT and ORI@FT (40.92% and 32.73%, respectively). Considering that high intracellular GSH concentrations in tumor cells tend to eliminate reactive oxygen species (ROS), the GSH-scavenging capacities of different DDSs were investigated. The GSH depletion potentials of FT and ORI@FT were relatively poor (Fig. 1I), indicating that CaO_2 also improved the GSH scavenging potential. Therefore, the FM@NPs contributed to GSH depletion and enhanced the efficacy of PDT and CDT. The potential of the different DDSs to improve the hypoxic environment was investigated in terms of O_2 generation. A portable dissolved O_2 meter was used to determine changes in O_2 content in anaerobic water exposed to different DDSs. As shown in Fig. S4, FT and ORI@FT did not exhibit changes in oxygen content over time. However, the oxygen content of the anaerobic water treated with DDSs containing CaO_2 increased from 0 to 2 mg/L within 12 h.

3.3. Drug-loading and pH-responsive release of drug

Calcium, iron, and ORI loading were determined using high-performance liquid chromatography (HPLC) and inductively coupled plasma mass spectrometry (ICP-MS). The drug-loading capacity (DLC) of ORI, calcium, and iron in FM@NPs were 6.31 ± 0.82%, 3.98 ± 0.15%, and 13.47 ± 0.19%, respectively (Supporting Information Table S1). Owing to the difference in the pH of the tumor microenvironment and physiological conditions, pH-responsive drug release properties were determined. As shown in Fig. 1J−L, after 12 h, at pH 5.5, almost 100% of ORI, calcium, and iron were released from FM@NPs. Furthermore, after 12 h, at pH 6.8, 48.57%, 23.96%, and 32.10% of ORI, calcium, and iron, respectively, were released from FM@NPs. Whereas at pH 7.4, after 12 h, only 10.64%, 4.86%, and 19.14% of ORI, calcium, and iron were released, respectively. These results demonstrated that FM@NPs can be used as efficient pH-responsive DDSs with controlled drug release (approximately 95% release) in the presence of GSH. This was because the low pH protonated the −COOH groups of TCPP, accelerating the stepwise dissolution of the CaO_2 inner core[43]. This system resulted in an effective combination of CMT, CDT, and PDT through a mechanism in which endogenous GSH reduced Fe^{3+} to Fe^{2+} and activated the Fenton reaction, whereas CaO_2 provided an O_2-rich environment, further promoting the efficacy of CDT and PDT.

3.4. Homologous targeting and subcellular localization

Studies have shown that coating the tumor and cell membranes of DCs results in the homologous targeting and immune escape of DDSs[44,45]. Given that FM contains the membrane proteins of B16-F10 cells, FM@NPs hold promise for effectively targeting B16-F10 cells. The targeting potential of the membrane-coated and non-membrane-coated DDSs in B16-F10 cells was evaluated using CLSM. As presented in Supporting Information Fig. S5, stronger fluorescence was observed in the B16-F10 cells treated with membrane-coated DDSs than in the cells treated with non-membrane-coated DDSs. The uptake of different DDSs by different cell lines, *i.e.*, HepG2 cells and normal human dermal fibroblasts (NHDF), was observed using CLSM (Supporting Information Figs. S6 and S7). After incubation for 8 h, HepG2 and NHDF cells showed uptake of FT, ORI@FT, CaO_2@FT, and NPs, potentially owing to the positive charge of them. However, after incubation with CM@NPs, DM@NPs, and FM@NPs for 8 h, no cell lines showed obvious red fluorescence,

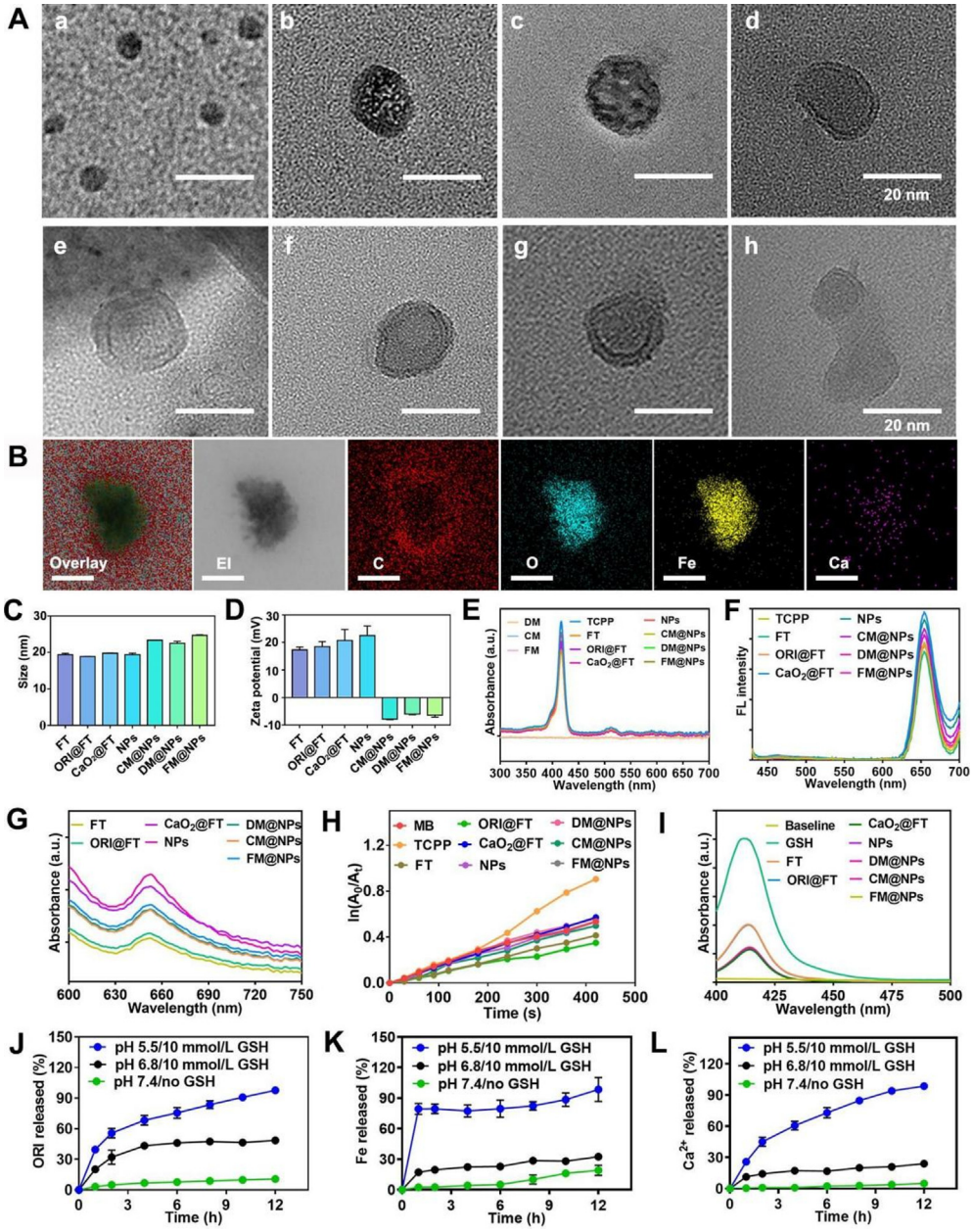

Figure 1 (A) TEM image of (a) CaO_2; (b) FT; (c) ORI@FT; (d) CaO_2@FT; (e) NPs; (f) DM@NPs; (g) CM@NPs; (h) FM@NPs; (B) TEM and EDX mapping images of FM@NPs; (C) Mean hydrodynamic diameter of FT, ORI@FT, CaO_2@FT, NPs, DM@NPs, CM@NPs, and FM@NPs in water; (D) Zeta potential of FT, ORI@FT, CaO_2@FT, NPs, DM@NPs, CM@NPs, and FM@NPs; (E) UV−Vis spectra of DM, CM, FM, TCPP, FT, ORI@FT, CaO_2@FT, NPs, DM@NPs, CM@NPs, and FM@NPs; (F) Fluorescence emission spectra of TCPP, FT, ORI@FT, CaO_2@FT, NPs, DM@NPs, CM@NPs, and FM@NPs; (G) UV−Vis spectra of ·OH produced by FT, ORI@FT, CaO_2@FT, NPs, DM@NPs, CM@NPs, and FM@NPs; (H) Photodegradation rates of DPBF in DMF induced by FT, ORI@FT, CaO_2@FT, NPs, DM@NPs, CM@NPs, and FM@NPs (A_0 is the initial absorbance of the phthalocyanine probe); (I) UV absorption curves of DTNB complexes with remaining GSH after FT, ORI@FT, CaO_2@FT, NPs, DM@NPs, CM@NPs, and FM@NPs reacted with 5 mmol/L GSH; (J) HPLC diagram of ORI release; (K) ICP-MS diagram of Iron release; (L) ICP-MS diagram of Ca^{2+} release. Error bars represented SD values ($n = 3$). * Indicates statistically significant differences ($^*P < 0.05$, $^{***}P < 0.001$).

indicating that HepG2 and NHDF showed little uptake of CM@NPs, DM@NPs, and FM@NPs. The analysis suggested that the three DDSs were all negatively charged and had different sources than receptor cells. This validated the data showing that the homologous binding properties of cancer cell membranes endowed DDSs with the capacity to target cancer cells. Owing to their positive surface charge, non-membrane-coated DDSs also showed some cellular affinity[46]. In addition, the iron and calcium contents in B16-F10 cells treated with different DDSs may be used as parameters to determine the uptake efficiency (Fig. 2A, Supporting Information Figs. S8 and S9). Intracellular iron and calcium content increased after treatment with membrane-coated DDSs. As shown in Supporting Information Figs. S10 and S11, CLSM was used to determine the subcellular localization of the

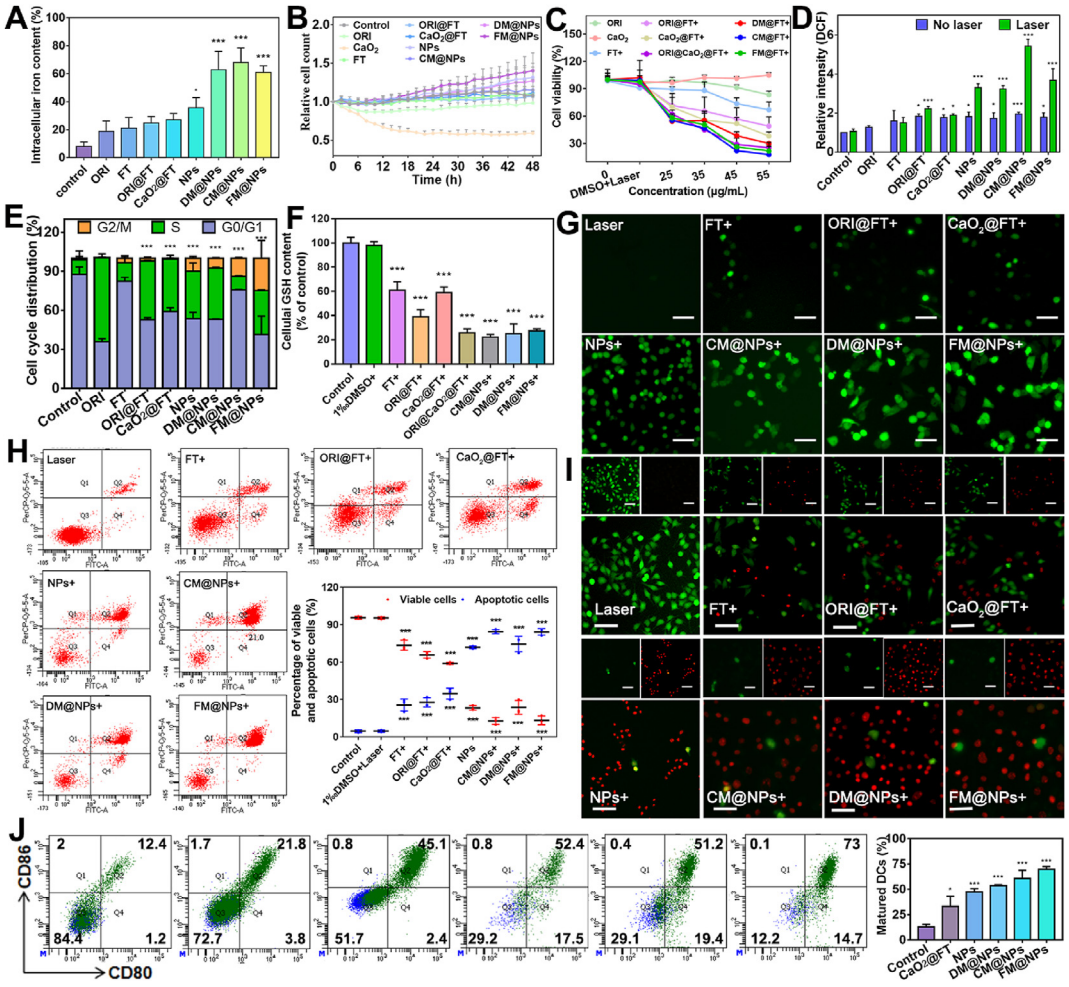

Figure 2 (A) Intracellular iron content in B16-F10 cells incubated with different nanoformulations; (B) Cell proliferation of BMDCs treated with different nanoparticles for 48 h; (C) Relative viabilities of B16-F10 cells post various treatments as indicated for 24 h; (D) Analysis of ROS generation using the oxidant sensitive fluorescent probe DCFH-DA; (E) Cell cycle distribution of B16-F10 cells treated with different DDSs for 24 h; (F) Intracellular GSH content in B16-F10 cells after incubation with different NPs + laser irradiation; (G) CLSM images of intracellular ROS detected by DCFH-DA probe. Scale bar = 30 μm; (H) Apoptosis detection of B16-F10 cells; (I) The LIVE/DEAD staining images of B16-F10 cells after different treatments. Scale bar = 100 μm; (J) The expression of CD80 and CD86 in DCs quantified by flow cytometry after different treatments. + represents irradiation using a 660 nm laser with a power intensity of 75 mW/cm^2 for 4 min. Error bars represented SD values (n = 3). * Indicates statistically significant differences (*P < 0.05, ***P < 0.001).

different nanoformulations. Red fluorescence of FT was observed in the lysosomes and mitochondria. These results indicate that the synthesized DDSs were widely distributed in the cytoplasm and exerted anti-tumor effects.

3.5. *Cytotoxicity and anti-tumor mechanisms study*

The viability of B16-F10 cells was determined using a cell counting kit-8 (CCK-8) assay to evaluate the cytotoxicity of the different DDSs[47]. B16-F10 cells treated with different FT concentrations showed >90% viability (Supporting Information Fig. S12), thereby indicating good biocompatibility of FT. At the same time, the safety of different DDSs for DCs was also evaluated. The proliferation experiment results showed that both NPs and membrane-modified NPs induced the proliferation of DCs, indicating that the DDSs were safe and enhanced immunity (Fig. 2B). However, CaO_2 is not safe and significantly inhibits DC proliferation. The optimal laser parameters for cell experiments were determined to be the intensity of 75 mW/cm^2 and a duration of 4 min (Supporting Information Fig. S13). The cytotoxicity of each DDS (dark or light) was determined *in vitro*. Fig. 2C and Fig. S12 show that all the drugs resulted in a dose-dependent decrease in cell viability. Compared with the control group, the cell viability of each group treated with ORI, FT, or FT + laser decreased, but the killing effect on the cells was still insufficient. The cytotoxicity in the NPs+laser group was significantly increased by the combined action of CMT, CDT, and PDT. The CM@NPs+laser group exhibited the highest cytotoxicity. The introduction of CaO_2 produced H_2O_2 and O_2 and enhanced the efficacy of CDT-PDT, resulting in significant cell inhibitory efficiency. The CMT-CDT-PDT combination therapy was more advantageous than CMT or CDT alone. AnnexinV−FITC and live/dead cell staining were used to further determine the cell viability in each group, and living and dead cells were distinguished using green and red fluorescence, respectively (Fig. 2H and I, and Supporting Information Figs. S14 and S15). However, the effect of

laser irradiation on the cell viability was not significant. The NPs and membrane-coated NPs group showed obvious cytotoxicity, which was further enhanced after exposure to light, consistent with the results of the CCK-8 assay. These findings further validate the advantages of the synergistic CMT-CDT-PDT ion interference technique. Furthermore, changes in the cell cycle of B16-F10 cells treated with different drugs for 24 h were analyzed using flow cytometry (BD FACSCanto II, USA, Fig. 2E). It was found that the NPs promoted S-phase arrest. At the same time, the mitochondrial membrane potential (MMP) was determined using flow cytometry. The MMP decreased after the introduction of ORI and CaO_2 (Supporting Information Fig. S16). In addition, laser radiation caused a greater decrease in the MMP.

Based on the anticancer mechanism of Ca^{2+}, it may be speculated that the increased lethality of the CM@NPs + laser group was related to the additional Ca^{2+} provided by the degradation of CaO_2[27]. Increased cytosolic Ca^{2+} concentration results in improved oncosis efficiency. B16-F10 cells were imaged under biological transmission electron microscopy (Bio-TEM) to confirm cell morphology. As shown in Supporting Information Figs. S17 and S18, the cells in the control and laser-treated groups remained viable, with no significant morphological changes. The membranes of ORI-treated cells were budding, indicating apoptosis. Cells treated with NPs became swollen and enlarged due to the introduction of Ca^{2+}. More importantly, the cells did not have an intact shape after exposure to light, and the plasma membranes were broken, indicating necrotic apoptosis. These results confirm the hypothesis that the integration of CMT, PDT, CDT, and ion interference techniques into a biological platform may result in improved anti-tumor effects. In addition, the lipid ROS levels were determined using C11-BODIPY581/591 to investigate whether each preparation induced ferroptosis (Supporting Information Figs. S19 and S20). Stimulation with different preparations increased lipid ROS content in B16-F10 cells, confirming that ferroptosis was induced by ORI and iron.

To further identify the cause of drug-induced cell death, several inhibitors of different cell death pathways were used[19]. First, the safety of E 64 (a proteinase inhibitor), Necrostatin 1 (a necrosis inhibitor), Z-VAD-FMK (a pan-cysteine protease inhibitor) and Ferrostatin 1 (a ferroptosis inhibitor) in cells was determined (Supporting Information Fig. S21). The combination of different inhibitors and therapeutic agents revealed that ferroptosis and apoptosis were the main mechanisms underlying ORI-induced cell death (Supporting Information Fig. S22). However, cell death induced by NPs and FM@NPs was not reversed by any cell death inhibitor, indicating that the anti-tumor effects of the different DDSs were mediated through multiple modes of cell death (Supporting Information Figs. S22 and S23). This is also beneficial for the effective killing of tumor cells and the dismantling of the self-protection mechanism of tumors. These findings fully demonstrate the advantages of the CMT-CDT-PDT-ion interference technology integration platform as an anti-tumor strategy.

First, the potential of different agents to ameliorate hypoxia was investigated by measuring the intracellular oxygen content using the intracellular oxygen indicator $[Ru(DPP)_3]Cl_2$, the fluorescence of which is quenched in reaction with oxygen molecules. Compared to the FT+ laser group, B16-F10 cells treated with NPs and FM@NPs showed varying degrees of attenuation of red fluorescence (Supporting Information Figs. S24 and S25), thereby confirming that the CaO_2-induced catalytic reaction produced significant oxygen in the cells and successfully improved the intracellular anoxic environment. After confirming the improvement in intracellular hypoxia, the efficacies of PDT and CDT were evaluated. To this end, 2′,7′-dichlorofluorescin diacetate (DCFH-DA) was used to determine the production of reactive oxygen species (ROS) in B16-F10 cells treated with different DDSs. Compared to the PBS group, the intracellular fluorescence intensity of B16-F10 cells treated with each DDS was enhanced to a certain extent (Fig. 2D and G, and Supporting Information Fig. S26). A distinct green fluorescence indicated the production of ·OH through the Fenton reaction as a result of the reduction of Fe^{3+}. As shown in Fig. 2D, the levels of ROS produced by the NPs increased significantly with the introduction of ORI and CaO_2. This may be due to H_2O_2-enhanced CDT generation *via* CaO_2 decomposition and ORI-induced GSH depletion. In addition, the fluorescence intensity of each group after illumination was significantly enhanced compared with that of the unilluminated group, indicating that a large amount of O_2 was produced in the cells after illumination. Therefore, it can be stated that FM@NPs are expected to exhibit a good tumor-killing effect under irradiation. The efficacy of CDT depends on the ability of FM@NPs to produce ·OH. Therefore, the potential of different formulations to induce ·OH production in B16-F10 cells was evaluated using CLSM. As shown in Supporting Information Figs. S27 and S28, cells treated with different DDSs showed significant red fluorescence when compared with control cells, indicating that the FM@NPs effectively produced ·OH. In addition, the introduction of CaO_2 improved the efficiency of the Fenton reaction and boosted the production of ·OH. To confirm this hypothesis, the amount of intracellular GSH produced after different DDS treatments was determined. As shown in Fig. 2F and Supporting Information Fig. S29, the intracellular GSH levels in cells treated with ORI and FM@NPs were significantly reduced when compared with the control cells.

3.6. *In vitro immune response*

As FM expresses all antigens in B16-F10 cells, it can be reasonably speculated that FM@NPs may induce an immune response[27]. Therefore, the immune-stimulatory activity of different DDSs on bone marrow dendritic cells (BMDCs) was investigated. The expression levels of specific co-stimulatory molecules (CD80 and CD86) on the membranes of BMDCs were determined using flow cytometrically (Fig. 2J). The percentage of mature BMDCs co-cultured with FM@NPs was significantly higher than that in other groups (Fig. 2J). In addition, the maturation of DC induced by CM@NPs was stronger than that induced by DM@NPs. Moreover, compared to the controls, NPs induced an immune response, which may be related to inflammation induced by oncosis and ferroptosis.

PDT can induce powerful ICD effects through the release of damage-associated molecular patterns (DAMPs), thus activating anti-tumor immunity, such as cell surface exposure to calreticulin (CRT), extracellular release of adenosine triphosphate (ATP), and high-mobility group box 1 (HMGB1)[48]. Therefore, we evaluated the effects of different treatments on B16-F10 cells by measuring CRT exposure, HMGB1 levels, and ATP efflux. CRT expression in B16-F10 cells was detected using immunofluorescence staining. The CLSM image shows (Fig. 3A and Supporting Information Fig. S30) that the green fluorescence on the surface of B16-F10 cells indicates effective exposure to CRT. No obvious

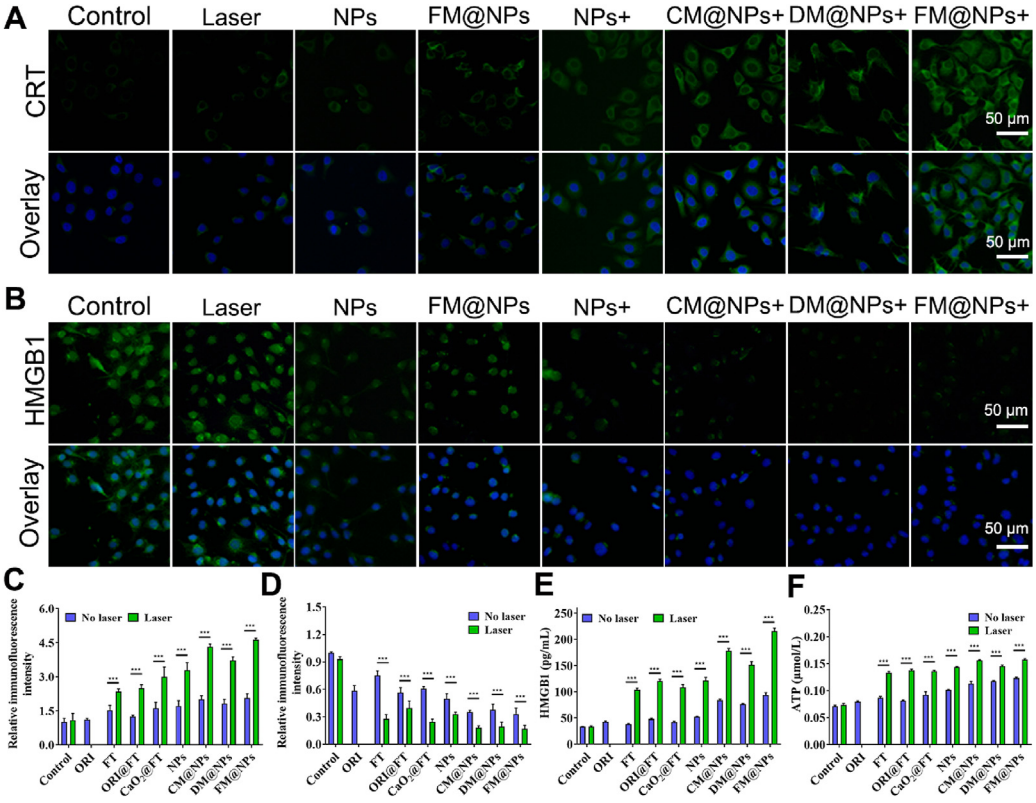

Figure 3 (A) CRT immunofluorescence staining, the cell nuclei were stained by DAPI; (B) HMGB1 immunofluorescence staining, the cell nuclei were stained by DAPI; (C) the quantitative fluorescence analysis of CRT in B16-F10 cells after various treatments with or without laser irradiation; (D) the quantitative fluorescence analysis of HMGB1 in B16-F10 cells after various treatments with or without light irradiation. (E) Quantitative Elisa analysis of the released HMGB1 and (F) ATP release from B16-F10 cells under various treatments with or without light irradiation. + represents irradiation using a 660 nm laser with a power intensity of 75 mW/cm^2 for 4 min. Error bars represented SD values ($n = 3$). * Indicates statistically significant differences ($^*P < 0.05$, $^{***}P < 0.001$).

surface-exposed CRT was observed in B16-F10 cells treated with NPs+, CM@NPs+, DM@NPs+, and FM@NPs+. The absence of light treatment after administration resulted in a weak CRT surface exposure. Notably, FM@NPs+ induced the highest CRT content on the surface of B16-F10 cells. This is due to enhanced cellular internalization based on cell membrane-mediated homologous targeting. Next, CRT immunofluorescence was quantitatively analyzed (Fig. 3C). Compared to FM@NPs, FM@NPs+ increased the green fluorescence intensity of cells, which strongly confirmed its effectiveness in inducing ICD. Intracellular immunofluorescence and extracellular excretion of HMGB1 were detected by CLSM and enzyme-linked immunosorbent assay (ELISA). The CLSM images showed that HBGM1 was mainly expressed in the cells treated with DDS without laser irradiation (Fig. 3B– and D, and Supporting Information Fig. S31). The release of HMGB1 into the extracellular culture medium induced by FM@NPs+ was the most significant compared to the other groups (Fig. 3E). The extracellular release of ATP, shown in Fig. 3F, is consistent with the results of HMGB1 export. ATP ELISA results showed that FM@NPs+ has the potential to induce ATP secretion owing to the enhancement of the ICD effect by PDT through the reprogrammed metabolism of tumor cells. In summary, FM@NPs showed good PDT-mediated ICD performance under laser irradiation, demonstrating the advantages of tumor metabolic reprogramming combined with PDT.

3.7. *In vivo imaging*

Fluorescence imaging was performed in tumor-bearing mice using CY5.5, an imaging agent, at 4, 8, and 12 h after injection of DM@NPs, CM@NPs, and FM@NPs[49]. As shown in Fig. 4A, tumor-bearing mice injected with CM@NPs showed the strongest fluorescence at the tumor site, especially 12 h after injection, indicating that coating with cancer cell membranes enhanced effective retention at the tumor site. In addition, the FM@NPs showed superior tumor-targeting capacity, which may be due to the partial retention of CM by the FM@NPs. Twelve hours after the injection of different DDSs, fluorescence imaging of the main organs showed that fluorescence in the tumors of the membrane-coated DDS group was stronger than that in the other organs. This indicated that the membrane-coated NPs showed good tumor-targeting potential (Fig. 4B and C). NPs without a cell membrane coating also show tumor-targeting potential, which may be related to the enhanced permeability and retention effects (EPR effect) of the NPs[50].

3.8. *In vivo biosafety evaluation*

Haemolysis tests showed that different preparations had different effects on red blood cells (Supporting Information Fig. S32). The highest haemoglobin release was observed in a concentration-dependent manner in the FT group. There was almost no

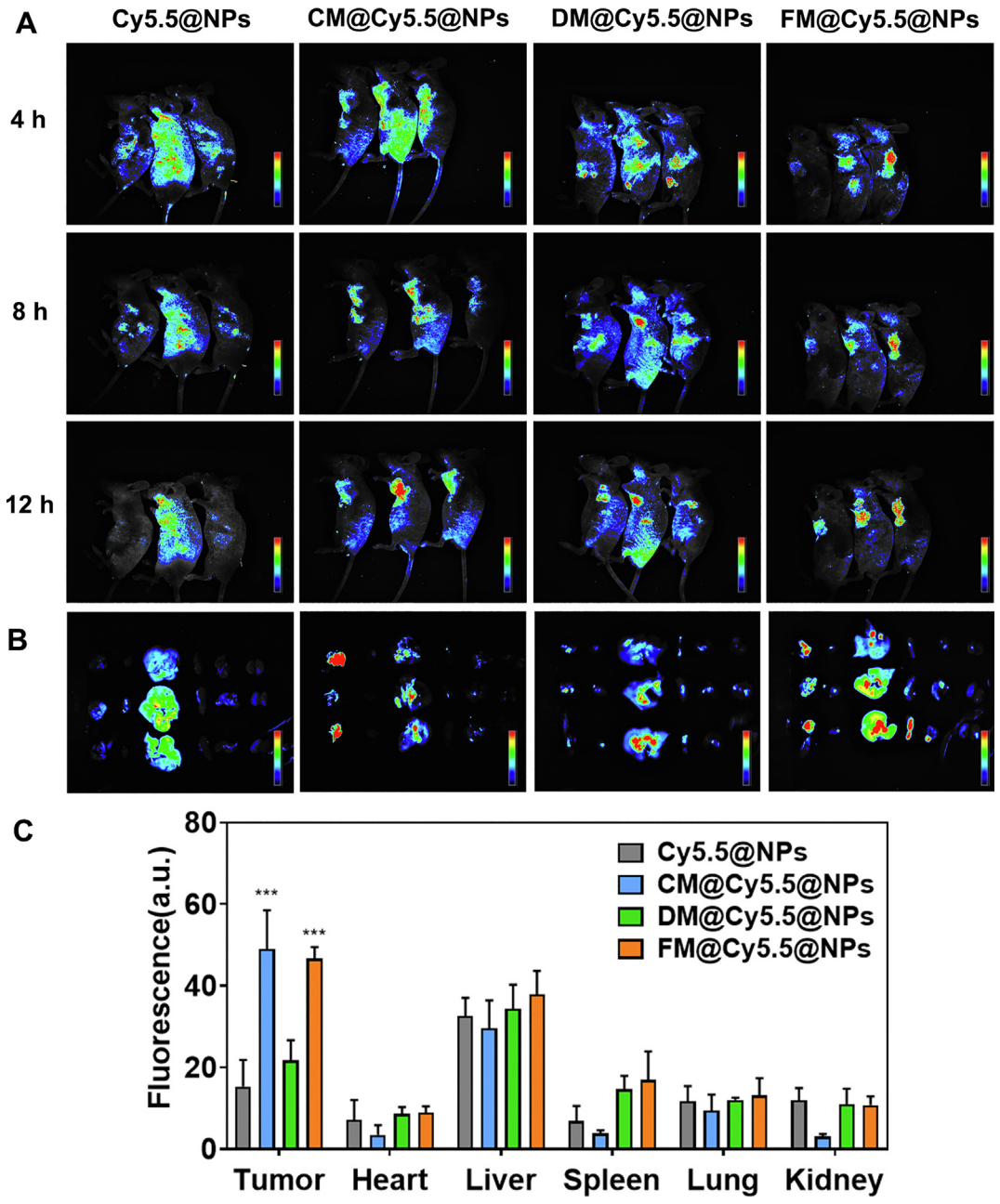

Figure 4 (A) *In vivo* biodistribution images of Cy5.5-labeled DDSs at 4, 8, and 12 h; (B) Fluorescence distribution images of tumor and different organs at 12 h after injection; (C) 12 h after the injection of different DDSs, fluorescence values of tumor and different organs after injection. Error bars represented SD values ($n = 3$).

haemolytic effect in the mice administered the other preparations, indicating that all preparations, except FT, had good biological safety. Subsequently, B16-F10 tumor-bearing mice were established. The body weights of mice were recorded daily during the treatment period. Mice in the treated groups showed a slight increase in mean body weight (Fig. 5B and C), but their weights were comparable to the mean weight of mice in the control group, indicating that each preparation had good biosafety. Six days after treatment, the major organs of the mice were excised and subjected to histological analysis using haematoxylin and eosin (H&E) staining. No obvious physiological abnormalities were observed in the major organs of mice in each group (Supporting Information Figs. S33−S37). To further confirm the *in vivo* safety of each preparation in mice, haematological parameters and biochemical indices were determined. The values of these parameters in each group were similar to those in the control group (Supporting Information Tables S2 and S3), indicating that all preparations had good biocompatibility.

3.9. *In vivo anti-tumor efficacy*

To study the anti-tumor effects of different preparations, a B16-F10 tumor-bearing mouse model was established and injected with normal saline, FT, ORI@FT, CaO_2@FT, NPs, CM@NPs, DM@NPs, or FM@NPs. Laser radiation and non-radiation groups were then established, and the therapeutic effect was determined.

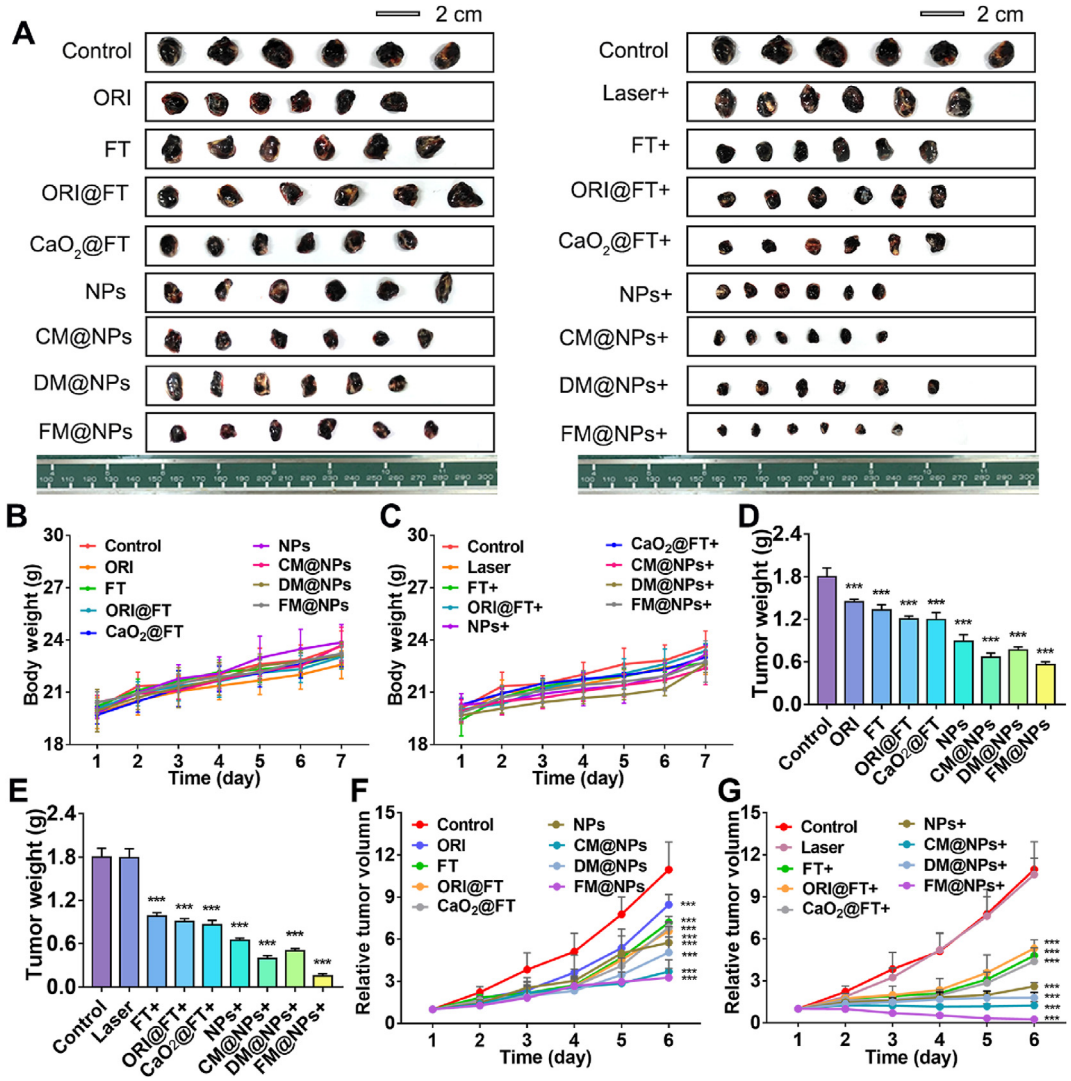

Figure 5 (A) Images of the tumor after 6 days of treatment; (B) Changes in body weight of tumor-bearing mice during drug administration; (C) Changes in body weight of tumor-bearing mice during drug administration; (D) Tumor weight after 6 days of treatment with different preparations; (E) Tumor weight after 6 days of treatment with different preparations + laser; (F) Relative tumor volume changes during treatment; (G) Relative tumor volume changes during treatment + laser. + represents irradiation using a 660 nm laser with a power intensity of 75 mW/cm^2 for 4 min. Error bars represented SD values ($n = 6$). * Indicates statistically significant differences (*$P < 0.05$, ***$P < 0.001$).

After 6 days of treatment, the tumors were excised and photographed. As shown in Fig. 5A, the FM@NPs + laser group exhibited better tumor growth inhibition than the other groups. This may be related to the synergistic effect induced by FM@NPs, especially the strong immune response, which makes FM@NPs more effective than CM@NPs. The tumor growth-inhibitory effects of the treatments were in the following order: FM@NPs > CM@NPs > DM@NPs > NPs > CaO_2@FT > ORI@FT > FT > ORI. The antitumor effect of the laser group was significantly better than that of the non-laser irradiation group. The trends observed in the visual analyses were also consistent with the results of the weight and volume analyses of the tumors (Fig. 5D–G). A terminal dinucleotide transferase-mediated incision end labelling (TUNEL) assay and H&E staining were performed after 6 days of treatment, and the results are shown in Supporting Information Fig. S38–S40. The results from H&E staining showed that laser irradiation produced a more significant tumor-killing effect than non-laser irradiation, and the FM@NPs+laser group produced the most obvious anti-tumor effect, which was consistent with the treatment results. The TUNEL assay showed that the FM@NPs+laser group exhibited the most intense tumor cell apoptosis.

The results of RT-qPCR and Western blot analysis proved that the anti-tumor activity of different DDSs was closely related to ferroptosis and the induction of abnormal iron transport and lipid metabolism in tumor tissue. The expression levels of iron transport-related markers (*i.e.*, *Hspb1*, *Tfr1*, *Pcbp1*, *Ireb2*), the expression levels of lipid metabolism-related markers (*i.e.*, *Fsp1*, *Coq10*, *Lpcat3*), and the expression levels of ferroptosis-related markers (*i.e.*, *Gpx4*, *Slc7a11*, *Acsl4*) were assayed. *Hspb1* expression plays a key role in the ferrostatin pathway. The deletion of *Hspb1* enhanced erastin-induced ferroptosis, whereas overexpression of *Hspb1* inhibited erastin-induced ferroptosis[51]. In addition, *Tfr1*, *Pcbp1*, *Ieb2*, *Fsp1*, *Coq10*, *Lpcat3*, *Gpx4*, *Slc7a11*, and *Acsl4* are involved in regulating the ferrostatin process[52–57]. mRNA and protein expression levels in the treatment groups were significantly different from those in the control group.

After treatment with various drugs, compared with the control group, the expression of *Tfr1* and *Steap3* in tumor tissues was significantly increased, and the expressions of *Hspb1*, *Pcbp1*, and *Ireb2* was significantly decreased; this trend was more significant in the CM@NPs and FM@NPs groups (Supporting Information Fig. S41A). Further comparison of the regulatory effects of various drugs on lipid metabolism-related mRNA showed that all drugs could induce changes in the expression of lipid metabolism-related mRNA in the tumor tissues of tumor-bearing mice. As shown in Fig. S41B, after treatment with different drugs, the expression of *Fsp1* and *Coq10* in tumor tissues was significantly decreased, while the expression of *Lpcat3* was significantly increased compared to that in the control group; this trend was more significant in the CM@NPs and FM@NPs groups. In addition, after treatment with different DDSs, the expression of *Gpx4* and *Slc7a11* in tumor tissues was significantly decreased, whereas the expression of *Acsl4* significantly increased compared to the control group (Supporting Information Fig. S42). The effects of different drugs on iron transport and lipid metabolism-related protein expression in the tumor tissues of tumor-bearing mice were investigated by western blotting (Fig. 6A and B). The protein expression results were consistent with those of the mRNA, which indicated that DDS played an anti-tumor role by inducing ferroptosis. The combination of ORI and Fe-based MOF amplified ferroptosis induced by ORI and FT. The relative content of Fe^{2+} in the serum was further detected, as shown in Supporting Information Fig. S43. Compared to the control group, the relative concentration of Fe^{2+} in the serum of all groups was significantly increased. There was no significant difference in the relative serum concentrations of Fe^{2+} between the FT and control groups; furthermore, the relative serum concentration of Fe^{2+} in the CM@NPs and FM@NPs groups showed the most obvious increase, indicating that the CM@NP, DM@NP, and FM@NP groups had good targeting. The incorporation of ORI allowed the iron ions to enter the cells, but they could not be expelled in time, thereby inducing ferroptosis.

The number of tumor-infiltrating $CD3^{+}CD8^{+}$T cells was measured (Supporting Information Figs. S44 and S45). Following

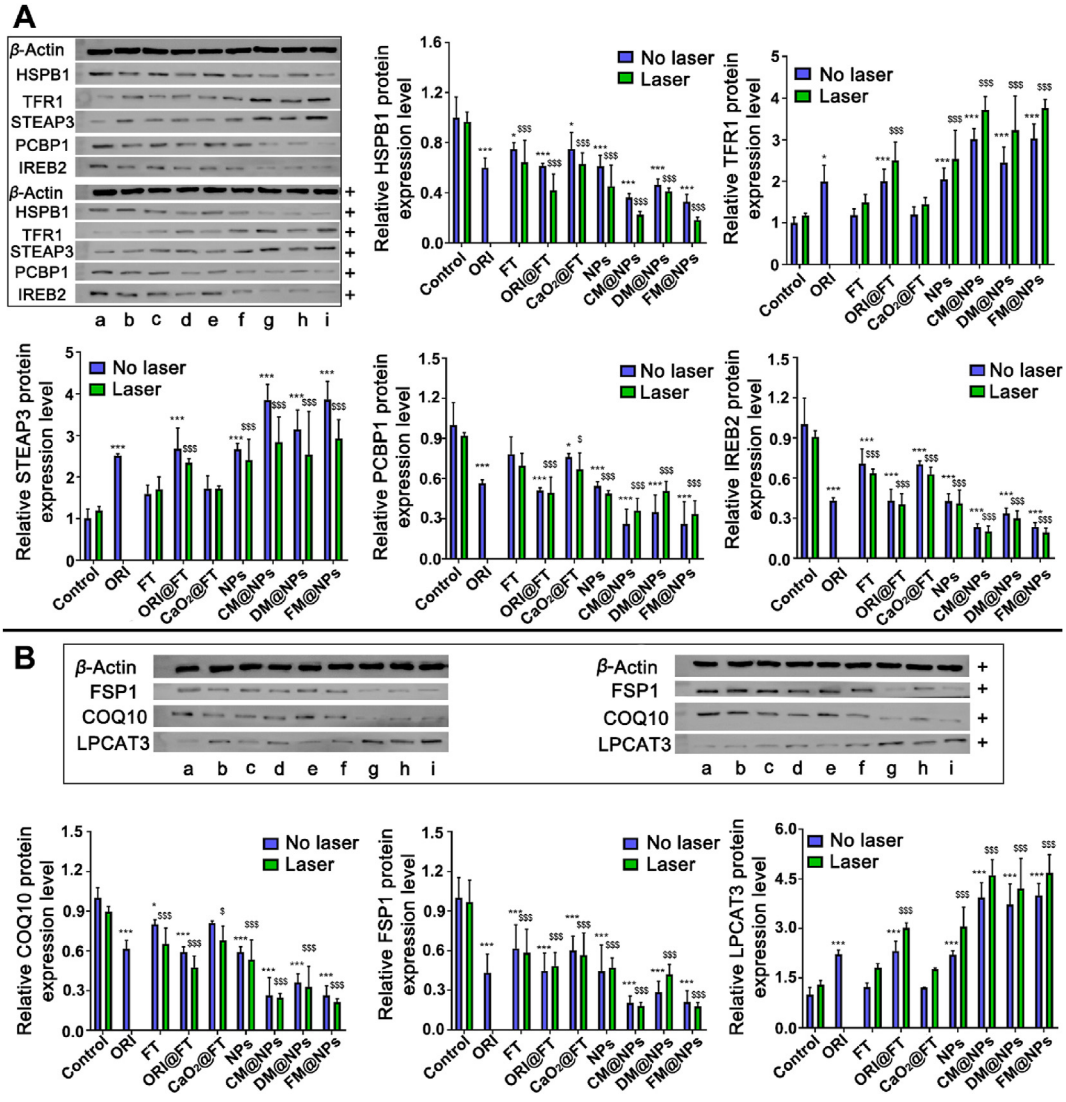

Figure 6 Effects of different drugs on the expression of (A) iron transport and (B) ferroptosis related protein (HSPB1, TFR1, STEAP3, PCBP1, IREB2, FSP1, COQ10, LPCAT3) in B16-F10 melanoma. (a) Control; (b) ORI; (c) FT; (d) ORI@FT; (e) CaO_2@FT; (f) NPs; (g) CM@NPs; (h) DM@NPs; (i) FM@NPs ($n = 3$). * Indicates statistically significant differences ($^{*}P < 0.05$, $^{***}P < 0.001$).

the administration of FM@NPs and laser irradiation, the tumors showed high $CD3^+$ and $CD8^+$ expression levels, indicating a strong immune response. In contrast, the CM@NPs and DM@NPs groups exhibited mild immune responses. Even in the absence of laser irradiation, the FM@NPs significantly enhanced the accumulation of $CD3^+CD8^+$T cells. It is postulated that CD86 may potentially be a marker of DCs' maturation and that it may provide a signal for the activation of T cells, while IFN-γ and TNF-α may activate the immune system and mediate the activity of immune cells. Therefore, immunofluorescence assay for CD86, IFN-γ, and TNF-α was used to study the maturation of DCs and the secretion of immune factors after the different treatments. As shown in Supporting Information Figs. S46–S48, the CD86 expression level was highest in mice in the FM@NPs group. Significant DC maturation was induced by FM@NPs even in the absence of laser irradiation, suggesting that FM@NPs induced strong anti-tumor immunity. In addition, due to the secretion of IFN-γ, caspase-3 was activated, leading to the initiation of the apoptotic and anti-tumor effects. Therefore, the present study also determined the expression of Caspase-3 in tumors (Supporting Information Fig. S49). The expression level of Caspase-3 had the same trend as those of IFN-γ and other immune factors. In addition, PDT-induced immunotherapy can be further enhanced by the inter-tumor ICD effects. Therefore, the *in vivo* ICD effects were estimated by measuring intertumor CRT exposure using immunofluorescence staining. As shown in Supporting Information Figs. S50 and S51, FM@NPs+ induced the highest CRT exposure and the lowest HMGB1 exposure *in vivo*, indicating its superior performance in inducing ICD. The major cytokines that reflect the activation of the immune system are IFN-γ, IL-1β, IL-4, IL-6, IL-12 (P70), and TFN-α. These cytokines regulate antigen presentation and control antiproliferative and anti-angiogenic effects. To verify whether the different preparations induced systemic immunity *in vivo*, serum cytokine levels were determined. As shown in Supporting Information Fig. S52, the expression levels of all cytokines increased to varying degrees, indicating activation of systemic immunity in mice.

3.10. Biodistribution and clearance of FM@NPs: iron and calcium

The biological distribution of iron and calcium was measured before, after 6 days, and after 30 days of administration to determine whether there was an accumulation of metal elements *in vivo*. After 6 days of intravenous injection, all tissues showed a certain degree of increased iron and calcium content (Fig. 7A–F). In particular, the content of calcium and iron in the tumor tissue significantly increased, indicating the precise targeting of FM@NPs. Iron and calcium levels in the liver and kidney increased significantly after 6 days of administration, mainly because they are metabolic and excretory organs. The liver and spleen, being part of the reticuloendothelial system (RES) tissues responsible for blood purification and iron homeostasis, showed a significant increase in iron concentrations 6 days after injection. This can be explained by the well-known process of "opsonization" of foreign particles, in which immune serum proteins called

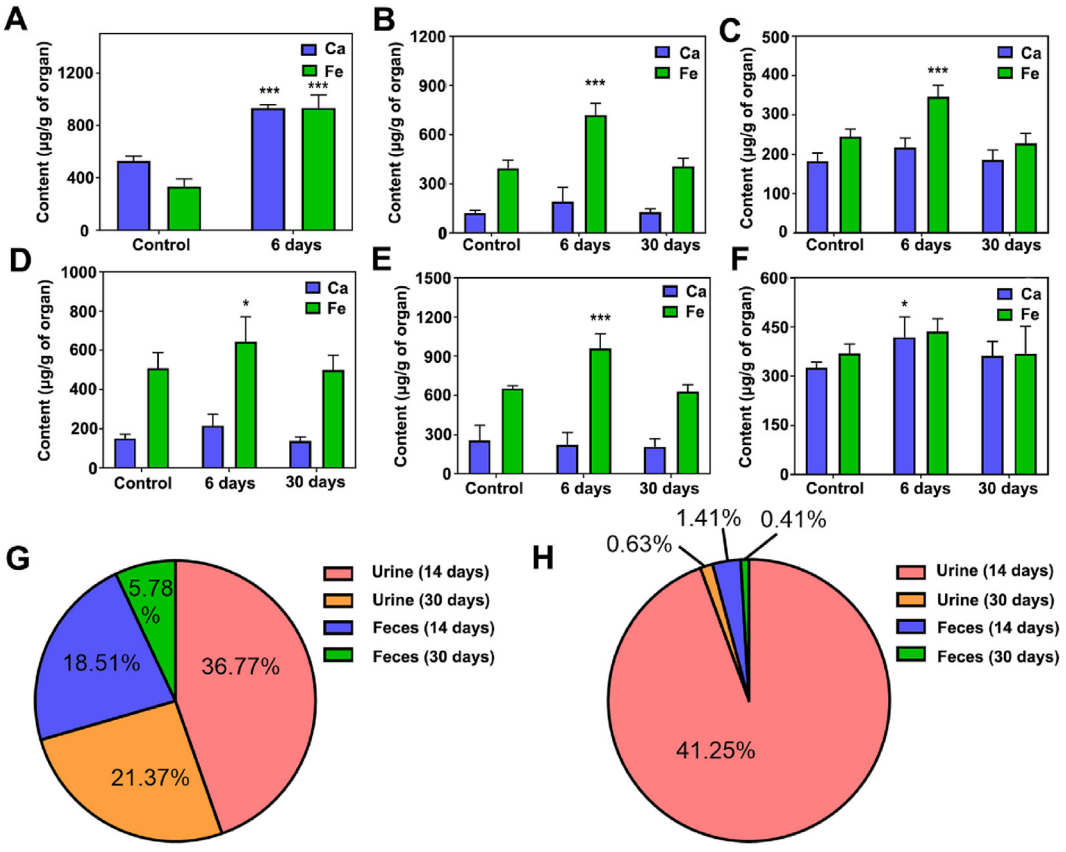

Figure 7 Calcium and iron levels in (A) tumor; (B) liver; (C) kedneys; (D) heart; (E) spleen; (F) lung; (G) calcium excreted in urine and feces, and (H) iron excreted in urine and feces ($n = 6$). * Indicates statistically significant differences ($^*P < 0.05$, $^{***}P < 0.001$).

opsonins are adsorbed onto the surface of the particles, enabling macrophages to engulf them[58]. Notably, the iron and calcium levels, although somewhat elevated, remained below the safe doses reported in the literature. After 30 days of administration, the iron and calcium contents returned to normal values compared to those in the control group, which confirmed that the FM@NPs were excreted normally *in vivo*. Therefore, we measured iron and calcium levels in the urine and stool within two weeks and one month after administration. As depicted in Fig. 7G and H, most of the iron and calcium were excreted through the urine, indicating that the clearance of iron and calcium is related to the kidneys. This result further confirmed that FM@NPs were degraded and discharged from the body within a month without causing an accumulation of metals in the body.

4. Conclusions

In this study, a tumor-targeting nanobiotic platform was constructed to enhance anti-tumor efficacy through synergy between photodynamic therapy, chemodynamic therapy, immunotherapy, and ferroptosis. When the tumor cells internalized the platform, the external FT layer of the nano platform was degraded by the high concentration of GSH in a slightly acidic environment, thereby releasing Fe^{3+} and TCPP, resulting in the collapse of the frame structure. Under the condition of high levels of O_2 and H_2O_2 produced by CaO_2, the highly toxic O_2 and ·OH were produced *via* laser irradiation and Fenton reaction. In addition, the released ORI and Fe^{3+} cooperated to overload the intracellular iron and cause abnormal lipid metabolism, thereby inducing ferroptosis in tumor cells. The excellent homologous targeting ability of FM facilitated the aggregation of nanobiological platforms at tumor sites. Moreover, FM induced immunotherapeutic effect owing to the abundance of tumor antigens and immune co-stimulatory molecules. Therefore, the designed nanobiological platform with multiple therapeutic effects is a promising strategy for achieving effective tumor suppression while preventing tumor metastasis in melanoma.

Acknowledgments

This research was funded by the Young Elite Scientists Sponsorship Program by China Association of Chinese Medicine (No. CACM-QNRC2-A03, China), the Beijing Natural Science Foundation (No. 7202121, China), and the National Natural Science Foundation of China (No. 81703715).

Author contributions

Mengru Cai performed the experiments, analyzed the results and drafted the manuscript. Tingting Fu, Rongyue Zhu, Panxiang Hu and Jiahui Kong designed and participated in animal experiments. Shilang Liao, Yuji Du, and Yongqiang Zhang performed the cell safety and toxicity experiments. Changhai Qu and Xiaoxv Dong contributed to the general methodology. Xingbin Yin and Jian Ni co-supervised the project and designed the experiments. All of the authors have read and approved the final manuscript.

Conflicts of interest

The authors have no conflicts of interest to declare.

Appendix A. Supporting information

Supporting information to this article can be found online at https://doi.org/10.1016/j.apsb.2024.05.015.

References

1. Schadendorf D, van Akkooi ACJ, Berking C, Griewank KG, Gutzmer R, Hauschild A, et al. Melanoma. *Lancet* 2018;**392**:971−84.
2. Adams R, Osborn G, Mukhia B, Laddach R, Willsmore Z, Chenoweth A, et al. Influencing tumor-associated macrophages in malignant melanoma with monoclonal antibodies. *Oncoimmunology* 2022;**11**:2127284.
3. Gray-Schopfer V, Wellbrock C, Marais R. Melanoma biology and new targeted therapy. *Nature* 2007;**445**:851−7.
4. Reits EA, Hodge JW, Herberts CA, Groothuis TA, Chakraborty M, Wansley EK, et al. Radiation modulates the peptide repertoire, enhances MHC class I expression, and induces successful antitumor immunotherapy. *J Exp Med* 2006;**203**:1259−71.
5. Reck M, Rodríguez-Abreu D, Robinson AG, Hui R, Csőszi T, Fülöp A, et al. Pembrolizumab versus chemotherapy for PD-L1-positive non-small-cell lung cancer. *N Engl J Med* 2016;**375**:1823−33.
6. Cukierman E, Khan DR. The benefits and challenges associated with the use of drug delivery systems in cancer therapy. *Biochem Pharmacol* 2010;**80**:762−70.
7. Peng H, Zhang X, Yang P, Zhao J, Zhang W, Feng N, et al. Defect self-assembly of metal-organic framework triggers ferroptosis to overcome resistance. *Bioact Mater* 2023;**19**:1−11.
8. Dixon SJ, Lemberg KM, Lamprecht MR, Skouta R, Zaitsev EM, Gleason CE, et al. Ferroptosis: an iron-dependent form of non-apoptotic cell death. *Cell* 2012;**149**:1060−72.
9. Yang WS, SriRamaratnam R, Welsch ME, Shimada K, Skouta R, Viswanathan VS, et al. Regulation of ferroptotic cancer cell death by GPX4. *Cell* 2014;**156**:317−31.
10. He H, Jiang H, Chen Y, Ye J, Wang A, Wang C, et al. Oridonin is a covalent NLRP3 inhibitor with strong anti-inflammasome activity. *Nat Commun* 2018;**9**:2550.
11. Li J, Wu Y, Wang D, Zou L, Fu C, Zhang J, et al. Oridonin synergistically enhances the antitumor efficacy of doxorubicin against aggressive breast cancer *via* pro-apoptotic and anti-angiogenic effects. *Pharmacol Res* 2019;**146**:104313.
12. Chen S, Cooper M, Jones M, Madhuri TK, Wade J, Bachelor A, et al. Combined activity of oridonin and wogonin in advanced-stage ovarian cancer cells: sensitivity of ovarian cancer cells to phyto-active chemicals. *Cell Biol Toxicol* 2011;**27**:133−47.
13. Zhang D, Zhou Q, Huang DD, He L, Zhang H, Hu B, et al. ROS/JNK/c-Jun axis is involved in oridonin-induced caspase-dependent apoptosis in human colorectal cancer cells. *Biochem Biophys Res Commun* 2019;**513**:594−601.
14. Fan X, Wang T, Ji Z, Li Q, Shen H, Wang J. Synergistic combination therapy of lung cancer using lipid-layered cisplatin and oridonin co-encapsulated nanoparticles. *Biomed Pharmacother* 2021;**141**:111830.
15. Gu H, Gwon MG, Kim JH, Jaechan Leem, Lee SJ. Oridonin attenuates cisplatin-induced acute kidney injury *via* inhibiting oxidative stress, apoptosis, and inflammation in mice. *BioMed Res Int* 2022;**2022**:3002962.
16. Song MQ, Liu XJ, Liu KD, Zhao R, Huang H, Shi YY, et al. Targeting AKT with oridonin inhibits growth of esophageal squamous cell carcinoma *in vitro* and patient-derived xenografts *in vivo*. *Mol Cancer Ther* 2018;**17**:1540−53.
17. Ding Y, Ding C, Ye N, Liu Z, Wold EA, Chen H, et al. Discovery and development of natural product oridonin-inspired anticancer agents. *Eur J Med Chem* 2016;**122**:102−17.
18. Zhang J, Wang N, Zhou Y, Wang K, Sun Y, Yan H, et al. Oridonin induces ferroptosis by inhibiting gamma-glutamyl cycle in TE1 cells. *Phytother Res* 2021;**35**:494−503.

19. Liu Y, Song Z, Liu Y, Ma X, Wang W, Ke Y, et al. Identification of ferroptosis as a novel mechanism for antitumor activity of natural product derivative a2 in gastric cancer. *Acta Pharm Sin B* 2021;**11**:1513−25.
20. Cui W, Zhang J, Wu D, Zhang J, Zhou H, Rong Y, et al. Ponicidin suppresses pancreatic cancer growth by inducing ferroptosis: insight gained by mass spectrometry-based metabolomics. *Phytomedicine* 2022;**98**:153943.
21. Chen Z, Yue Z, Yang K, Li S. Nanomaterials: small particles show huge possibilities for cancer immunotherapy. *J Nanobiotechnol* 2022;**20**:484.
22. Kamaly N, Xiao Z, Valencia PM, Radovic-Moreno AF, Farokhzad OC. Targeted polymeric therapeutic nanoparticles: design, development and clinical translation. *Chem Soc Rev* 2012;**41**:2971−3010.
23. Cheng K, Zhang Y, Li Y, Gao Z, Chen F, Sun K, et al. A novel pH-responsive hollow mesoporous silica nanoparticle (HMSN) system encapsulating doxorubicin (DOX) and glucose oxidase (GOX) for potential cancer treatment. *J Mater Chem B* 2019;**7**:3291−302.
24. Xue X, Qu H, Li Y. Stimuli-responsive crosslinked nanomedicine for cancer treatment. *Exploration* 2022;**2**:20210134.
25. Li SY, Cheng H, Xie BR, Qiu WX, Zeng JY, Li CX, et al. Cancer cell membrane camouflaged cascade bioreactor for cancer targeted starvation and photodynamic therapy. *ACS Nano* 2017;**11**:7006−18.
26. Rojas S, Arenas-Vivo A, Horcajada P. Metal-organic frameworks: a novel platform for combined advanced therapies. *Coord Chem Rev* 2019;**388**:202−26.
27. Wan X, Zhong H, Pan W, Li Y, Chen Y, Li N, et al. Programmed release of dihydroartemisinin for synergistic cancer therapy using a $CaCO_3$ mineralized metal-organic framework. *Angew Chem Int Ed Engl* 2019;**58**:14134−9.
28. Yang N, Cao C, Lv X, Zhang T, Shao J, Song X, et al. Photo-facilitated chemodynamic therapeutic agents: synthesis, mechanisms, and biomedical applications. *BMEMat* 2023;**1**:e12005.
29. Wu D, Zhu ZQ, Tang HX, Shi ZE, Kang J, Liu Q, et al. Efficacy-shaping nanomedicine by loading calcium peroxide into tumor microenvironment-responsive nanoparticles for the antitumor therapy of prostate cancer. *Theranostics* 2020;**10**:9808−29.
30. Suo M, Liu Z, Tang W, Guo J, Jiang W, Liu Y, et al. Development of a novel oxidative stress-amplifying nanocomposite capable of supplying intratumoral H_2O_2 and O_2 for enhanced chemodynamic therapy and radiotherapy in patient-derived xenograft (PDX) models. *Nanoscale* 2020;**12**:23259−65.
31. Zheng P, Ding J. Calcium ion nanomodulators for mitochondria-targeted multimodal cancer therapy. *Asian J Pharm Sci* 2022;**17**:1−3.
32. Zhang Y, Yang P, Wang XF. Microenvironmental regulation of cancer metastasis by miRNAs. *Trends Cell Biol* 2014;**24**:153−60.
33. Liu WL, Zou MZ, Liu T, Zeng JY, Li X, Yu WY, et al. Expandable immunotherapeutic nanoplatforms engineered from cytomembranes of hybrid cells derived from cancer and dendritic cells. *Adv Mater* 2019;**31**:e1900499.
34. Liu X, Liu Y, Li X, Huang J, Guo X, Zhang J, et al. ER-targeting PDT converts tumors into *in situ* therapeutic tumor vaccines. *ACS Nano* 2022;**16**:9240−53.
35. Koido S, Homma S, Okamoto M, Namiki Y, Takakura K, Takahara A, et al. Augmentation of antitumor immunity by fusions of ethanol-treated tumor cells and dendritic cells stimulated *via* dual TLRs through TGF-β1 blockade and IL-12p70 production. *PLoS One* 2013;**8**:e63498.
36. Koido S, Ohana M, Liu C, Nikrui N, Durfee J, Lerner A, et al. Dendritic cells fused with human cancer cells: morphology, antigen expression, and T cell stimulation. *Clin Immunol* 2004;**113**:261−9.
37. Su Y, Xu W, Wei Q, Ma Y, Ding J, Chen X. Chiral polypeptide nanoparticles as nanoadjuvants of nanovaccines for efficient cancer prevention and therapy. *Sci Bull* 2023;**68**:284−94.
38. Zheng Y, Han Yaobao, Sun Q, Li Z. Harnessing antitumor and tumor-tropism functions of macrophages *via* nanotechnology for tumor immunotherapy. *Exploration* 2022;**2**:20210166.
39. Xu W, Su Y, Ma Y, Wei Q, Yang J, Zhuang X, et al. Immunologically effective poly(D-lactic acid) nanoparticle enhances anticancer immune response. *Sci China Chem* 2023;**66**:1150−60.
40. Liu WL, Zou MZ, Liu T, Zeng JY, Li X, Yu WY, et al. Cytomembrane nanovaccines show therapeutic effects by mimicking tumor cells and antigen presenting cells. *Nat Commun* 2019;**10**:3199.
41. Dong ZL, Feng L, Hao Y, Li Q, Chen M, Yang Z, et al. Synthesis of $CaCO_3$-based nanomedicine for enhanced sonodynamic therapy *via* amplification of tumor oxidative stress. *Chem* 2020;**6**:1391−407.
42. Sun L, Xu Y, Gao Y, Huang X, Feng S, Chen J, et al. Synergistic amplification of oxidative stress-mediated antitumor activity *via* liposomal dichloroacetic acid and MOF-Fe^{2+}. *Small* 2019;**15**:e1901156.
43. Sun J, Jiang K, Wang Y, Liu Y, Wang T, Ding S, et al. One-pot synthesis of tumor-microenvironment responsive degradable nanoflower-medicine for multimodal cancer therapy with reinvigorating antitumor immunity. *Adv Healthc Mater* 2023;**12**:e2302016.
44. Yang R, Xu J, Xu L, Sun X, Chen Q, Zhao Y, et al. Cancer cell membrane-coated adjuvant nanoparticles with mannose modification for effective anticancer vaccination. *ACS Nano* 2018;**12**:5121−9.
45. Chen F, Geng Z, Wang L, Zhou Y, Liu J. Biomimetic nanoparticles enabled by cascade cell membrane coating for direct cross-priming of T cells. *Small* 2022;**18**:e2104402.
46. Ge Y, Zhang Y, Xia J, Ma M, He S, Nie F, et al. Effect of surface charge and agglomerate degree of magnetic iron oxide nanoparticles on KB cellular uptake *in vitro*. *Colloids Surf B Biointerfaces* 2009;**73**:294−301.
47. Zhu L, Kalimuthu S, Gangadaran P, Oh JM, Lee HW, Baek SH, et al. Exosomes derived from natural killer cells exert therapeutic effect in melanoma. *Theranostics* 2017;**7**:2732−45.
48. Liu Y, Wu H, Wang S, Zhang X, Gong L, Xiao C, et al. Biomimetic multifunctional nanodrugs enable regulating abnormal tumor metabolism and amplifying PDT-induced immunotherapy for synergistically enhanced tumor ablation. *Mater Today* 2023;**68**:125−47.
49. Akhavan O, Ghaderi E. Graphene nanomesh promises extremely efficient *in vivo* photothermal therapy. *Small* 2013;**9**:3593−601.
50. Fang J, Nakamura H, Maeda H. The EPR effect: unique features of tumor blood vessels for drug delivery, factors involved, and limitations and augmentation of the effect. *Adv Drug Deliv Rev* 2011;**63**:136−51.
51. Sun X, Ou Z, Xie M, Kang R, Fan Y, Niu X, et al. HSPB1 as a novel regulator of ferroptotic cancer cell death. *Oncogene* 2015;**34**:5617−25.
52. Zhang Jh, Xie LJ, Wang HL, Chen H, Meng X, Lin X, et al. Mechanism of ziyuglycoside II-mediated ferroptosis-related proteins on the proliferation and metastasis of human lung adenocarcinoma cell lines. *Pharmacogn Mag* 2023;**20**:7−15.
53. Tang X, Ding H, Liang Maoli, Chen X, Yan Y, Wan N, et al. Curcumin induces ferroptosis in non-small-cell lung cancer *via* activating autophagy. *Thorac Cancer* 2021;**12**:1219−30.
54. Pontel LB, Bueno-Costa A, Morellato AE, Carvalho Santos JC, Roué G, Esteller M. Acute lymphoblastic leukemia necessitates GSH-dependent ferroptosis defenses to overcome FSP1-epigenetic silencing. *Redox Biol* 2022;**55**:102408.
55. Gotorbe C, Durivault J, Meira W, Cassim S, Ždralević M, Pouysségur J, et al. Metabolic rewiring toward oxidative phosphorylation disrupts intrinsic resistance to ferroptosis of the colon adenocarcinoma cells. *Antioxidants* 2022;**11**:2412.
56. Reed A, Ichu TA, Milosevich N, Melillo B, Schafroth MA, Otsuka Y, et al. LPCAT3 inhibitors remodel the polyunsaturated phospholipid content of human cells and protect from ferroptosis. *ACS Chem Biol* 2022;**17**:1607−18.
57. Li FJ, Long HZ, Zhou ZW, Luo HY, Xu SG, Gao LC. System Xc-/GSH/GPX4 axis: an important antioxidant system for the ferroptosis in drug-resistant solid tumor therapy. *Front Pharmacol* 2022;**13**:910292.
58. Moghimi SMH, Hunter AC, Murray JC. Long-circulating and target-specific nanoparticles: theory to practice. *Pharmacol Rev* 2001;**53**:283−318.